ACS APPLIED MATERIALS & INTERFACES

Research Article

www.acsami.org

Influence of Chemical Composition and Structure in Silicon Dielectric Materials on Passivation of Thin Crystalline Silicon on Glass

Sonya Calnan,*,† Onno Gabriel,† Inga Rothert,† Matteo Werth,† Sven Ring,† Bernd Stannowski,† and Rutger Schlatmann†,‡

†PVcomB, Helmholtz-Zentrum Berlin für Materialien und Energie, Schwarzschildstraße 3, 12489 Berlin, Germany

‡Fachbereich 1 Ingenieurwissenschaften I, University of Applied Science (HTW) Berlin, Wilhelminenhofstraße 75 A, 12459 Berlin, Germany

Supporting Information

ABSTRACT: In this study, various silicon dielectric films, namely, a-SiO_x:H, a-SiN_x:H, and a-SiO_xN_y:H, grown by plasma enhanced chemical vapor deposition (PECVD) were evaluated for use as interlayers (ILs) between crystalline silicon and glass. Chemical bonding analysis using Fourier transform infrared spectroscopy showed that high values of oxidant gases (CO_2 and/or N_2), added to SiH_4 during PECVD, reduced the Si−H and N−H bond density in the silicon dielectrics. Various three layer stacks combining the silicon dielectric materials were designed to minimize optical losses between silicon and glass in rear side contacted heterojunction pn test cells. The PECVD grown silicon dielectrics retained their functionality despite being subjected to harsh subsequent processing such as crystallization of the silicon at 1414 °C or above. High values of short circuit current density (J_{sc}; without additional hydrogen passivation) required a high density of Si−H bonds and for the nitrogen containing films, additionally, a high N−H bond density. Concurrently high values of both J_{sc} and open circuit voltage V_{oc} were only observed when [Si−H] was equal to or exceeded [N−H]. Generally, V_{oc} correlated with a high density of [Si−H] bonds in the silicon dielectric; otherwise, additional hydrogen passivation using an active plasma process was required. The highest V_{oc} ~ 560 mV, for a silicon acceptor concentration of about 10^{16} cm^{-3}, was observed for stacks where an a-SiO_xN_y:H film was adjacent to the silicon. Regardless of the cell absorber thickness, field effect passivation of the buried silicon surface by the silicon dielectric was mandatory for efficient collection of carriers generated from short wavelength light (in the vicinity of the glass−Si interface). However, additional hydrogen passivation was obligatory for an increased diffusion length of the photogenerated carriers and thus J_{sc} in solar cells with thicker absorbers.

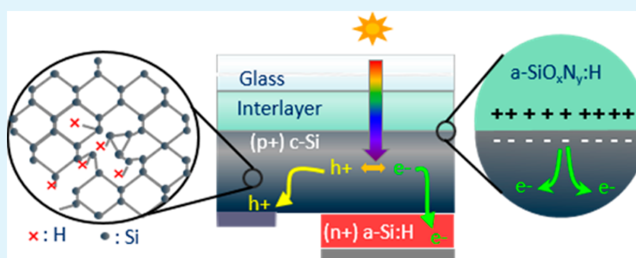

KEYWORDS: *crystalline silicon, passivation, silicon dielectrics, plasma enhanced chemical vapor deposition, liquid phase crystallization*

1. INTRODUCTION

Although crystalline silicon c-Si solar cells provide the highest efficiency to date, using widely abundant and low environmental impacting materials, a radical reduction of the material costs is imperative to compete with other conventional energy technologies. Solar cells made from thin c-Si on foreign low cost substrates such as glass, allow a reduction of both the material and energy costs with the promise of high photoconversion efficiency similar to c-Si wafers.

Thin film crystalline silicon (c-Si) on glass films is usually formed by growing amorphous silicon films by either sputtering,[1] chemical vapor deposition,[2−4] or electron beam evaporation,[1,5−9] followed by postdeposition using solid-phase crystallization (SPC)[2] or liquid-phase crystallization (LPC).[3,5,6] To date, higher values of solar cell open circuit voltage (V_{oc}) have been obtained by LPC compared to SPC of silicon.[10,11] In LPC, a laser[1,6,12] or an electron beam[3] is scanned over the silicon which melts for a short time and quickly cools to form crystals once the heating source has moved on. For this study laser-assisted LPC was used since it is performed under normal atmospheric conditions unlike e-beam crystallization that requires vacuum.

Despite the obvious cost advantages of thin crystalline silicon on glass compared to wafers, the achievement of high photoconversion efficiency devices comes with some challenges. Particularly, since the lateral grain size of LPC-Si on glass is similar to that typical of multicrystalline silicon wafers,[4,5,7,8] it is characterized by a high density of extended crystalline defects in the bulk such as intragrain dislocations, stacking faults, and twin boundaries as well as grain boundaries.[13] Considering the large size of grains, recombination at grain boundaries is expected to have a low influence on V_{oc}[14] and the efficiency appears to be dominated by the density of dislocations.[15] The density of recombination centers in the

Received: June 15, 2015
Accepted: August 17, 2015
Published: August 17, 2015

ACS Publications © 2015 American Chemical Society

Table 1. Deposition Parameters for Interlayer Component Materials

material	T_{sub} (°C)	RF power (W)	pressure (Pa)	SiH_4 flow (cm^3(STP) min^{-1})	H_2 flow (cm^3(STP) min^{-1})	CO_2 flow (cm^3(STP) min^{-1})	N_2 flow (cm^3(STP) min^{-1})
a-SiO_x:H	400	600	133	4−10	200	50−100	0
a-SiO_xN_y:H	400	600	133	10	200	0−100	500−1000
a-SiN_x:H	400	250−600	133−150	10−20	0−200	0	1000−1200

silicon bulk can be reduced by hydrogen passivation in which hydrogen is supplied and allowed to diffuse into the silicon where it saturates silicon dangling bonds. Also, since recombination of minority carriers at dislocations in multicrystalline silicon is enhanced by metal impurities,[16] diffusion of elements, such as iron, boron, sodium and potassium from the glass, must be blocked using a barrier. The abrupt termination of the silicon crystals and strain in the silicon bonds with the substrate causes silicon dangling bonds resulting in a high defect density. Although the best passivation of dangling bonds at the silicon surface is achieved by a-Si:H, this is inappropriate for LPC-Si, where the layer stack is subjected to temperatures around 1414 °C, the melting point of silicon. An alternative is to use field effect (FE) passivation via accumulation of a fixed charge in a dielectric layer which repels the majority photogenerated carriers in the silicon or by formation of an inversion zone in the silicon near the interface with the dielectric which, repels minority photogenerated carriers. In p-type Si, FE passivation can be achieved by negative charge accumulation in Al_2O_3 or via electrostatic generation of an inversion layer in the silicon by a positive fixed charge in silicon oxide (SiO_x), silicon nitride (SiN_x), or silicon oxynitride (SiO_xN_y). Other issues in LPC-Si on glass are related to the additional multiple functionality required from the mandatory interlayer (IL) which serves as a diffusion barrier. First, the diffusion barrier should also promote wetting and adhesion of the silicon to the glass both before and after the crystallization.[1,4,9] Second, if the solar cell is illuminated via the glass side, the IL should not only be transparent but also have a refractive index of around 2.2[17] to maximize in-coupling of light to the c-Si absorber. Lastly, the IL must retain all of the aforementioned properties even after exposure to high temperatures and several wet chemical etchings in postdeposition processing necessary to enhance the c-Si material quality and fabricate the solar cell.[4] However, no single material known to date can provide such varied functionality, and thus an IL consisting of a stack of different silicon dielectrics is favored.[4−6,8,9] The type and stacking order of the silicon dielectric used in such an interlayer is vital for high open circuit voltage in solar cells using LPC-Si on glass.[4−6,8] In previous studies, however, the SiO_x, SiN_x, and/or silicon carbide layers investigated for solar cells were grown either by RF sputtering only[5−8] or in combination with plasma enhanced chemical vapor deposition (PECVD),[5] which requires more than one deposition vacuum chamber. Since the silicon absorber precursor for the LPC-Si test cells used in this study was grown by PECVD, an interlayer consisting of SiO_x, SiN_x, and/or SiO_xN_y could be made in the same tool just by varying the precursor gas composition. This avoids a vacuum break and thus possible contamination of the sensitive interface between the IL and the silicon absorber. Also, PECVD is a well proven technique for uniform deposition on an industrially relevant substrate size above a 1 m^2 area.[2,18]

It is now appreciated that surface passivation by a silicon dielectric combined with bulk passivation using a hydrogen plasma is necessary to increase the solar cell efficiency of thin ≤10 μm thick c-Si on glass.[6,8,9,19] However, thus far, the influence of the chemical composition and structure of the passivating silicon dielectric material in combination with an additional hydrogen passivation of the c-Si on glass has not been specifically investigated. Therefore, in this contribution, we study the influence of varying the deposition parameters of PECVD grown a-SiO_x:H, a-SiN_x:H, and a-SiO_xN_y:H on their chemical composition and structure. We also compare the quality of field effect passivation of the buried silicon surface using a-SiO_x:H, a-SiN_x:H, and a-SiO_xN_y:H. In parallel, we present a study on the effect of varying the active plasma settings used for hydrogen passivation of the LPC- Si material on the short circuit current (J_{sc}) and V_{oc} of test solar cells. Finally, a correlation between the Si−H and N−H bond density of the silicon dielectric closest to the buried silicon surface and the J_{sc} and V_{oc} with and without additional hydrogen passivation is demonstrated.

2. MATERIALS AND METHODS

2.1. Deposition of a-SiO_x:H, a-SiO_xN_y:H, and a-SiN_x:H Interlayers. The a-SiO_x:H, a-SiO_xN_y:H, and a-SiN_x:H films were grown by PECVD in an AKT1600 cluster tool (Applied Materials) using process gas mixtures of SiH_4/H_2 with either CO_2 and/or N_2. The usage of N_2 as a nitrogen source for the PECVD of a-SiN_x:H layers is uncommon, because N_2 molecules need higher energies for dissociation compared to the more usually used NH_3. This is due to the different bond energies, which are 9.8 eV for N≡N in N_2 and only 4.7 eV for N−H in NH_3.[20] In this study, the more difficult dissociation of N_2 was compensated for by the admixture of very high amounts of N_2 to the process gas (typically, 1:100 SiH_4:N_2). Despite this drawback, the use of N_2 instead of NH_3 as a nitrogen source has the desirable effect of reducing the amount of bonded hydrogen in the films.[21−27]

CO_2 unlike N_2O or NO_2 is not commonly used as an oxygen source for the PECVD of a-SiO_x:H layers (again, the C═O bond energy is 5.5 eV compared to 3.2 eV for N═O[20]). Nevertheless, CO_2 has been extensively used in the PECVD of μc-SiO_x:H applied on optical windows layers and intermediate reflectors in a-Si:H/μc-Si:H-based thin film silicon solar cells[28−30] and for a-SiO_x:H as a passivation layer for c-Si.[31] One advantage of CO_2 over N_2O or NO_2 is that no additional nitrogen is incorporated into the a-SiO_x:H films,[27] while the films contain little or no carbon.[28−30] CO_2 is dissociated by collisions with electrons of sufficient energy, resulting in the production of atomic oxygen and CO, which is very stable in the plasma due to its high bond energy (11.2 eV). The atomic oxygen is either incorporated into the deposited a-SiO_x:H material or combines to form molecular oxygen which is pumped out of the reactor.

In order to obtain compact material, the density of hydrogen in the plasma originating from SiH_4 can be increased by admixing additional H_2 to the process gas.[4] All of the layers were grown with a substrate temperature (T_{sub}) of 400 °C as was used for the silicon absorber deposition. The other process parameters were varied over a range of values in order to adjust the properties of the different materials as summarized in Table 1.

2.2. Material Analysis of the a-SiO_x:H, a-SiN_x:H, and a-SiO_xN_y:H Layers. For the purpose of material analysis, the a-SiO_x:H, a-SiO_xN_y:H, and a-SiN_x:H films were grown with a nominal thickness of 200 nm on low conductivity double side polished Czochralski

DOI: 10.1021/acsami.5b05318
ACS Appl. Mater. Interfaces 2015, 7, 19282−19294

silicon wafers. The UV−visible reflectance of the layers on wafers was measured using a spectrophotometer (Lambda 1050, PerkinElmer) at near normal incidence. The thickness and refractive index of the silicon films were determined by fitting the reflectance, from 300 to 1100 nm, of an air/silicon dielectric/native SiO_x/silicon wafer stack using an optical model in SCOUT software.[32] It was necessary to add a thin SiO_x layer on the surface of the a-SiN_x:H films to achieve better fits. The dielectric function of each of the silicon dielectrics was described using a combination of a constant dielectric background caused by transitions at wavelengths below 300 nm and an OJL (O'Leary−Johnson−Lim) model[33] for the interband transitions close to the UV range. Dispersion spectra from the SCOUT database were used to represent the silicon wafer and native SiO_x in the optical model.

The mid-infrared (mid-IR) transmission and reflection spectra were recorded on the same spot using a Bruker Tensor 27 Fourier transform infrared (FTIR) system under nitrogen purging at room temperature with a spectral resolution of 4 cm^{-1} using 32 scans averaged per spectrum. The measured data were corrected for atmospheric absorption using OPUS 7 software. The film absorption coefficients were extracted by fitting the transmittance of a vacuum/silicon dielectric/native SiO_x/silicon wafer using an optical model in SCOUT.[32] Tabulated values available in the SCOUT material database were used for the silicon wafer and the native SiO_x. The dielectric function of the silicon dielectric was then modeled using the film thickness together with a constant dielectric background spectrum (for transitions at wavenumbers above 4000 cm^{-1}) overlaid by Brendel oscillators[34] to describe the vibrational modes. Thereafter, the absorption coefficient spectra were fitted using sums of peak components described by Gaussian area profiles with fityk software[35] in order to extract the positions, the full width at half-maximum and areal integrals of the peaks corresponding to vibrational modes. The various vibrational modes and positions were identified using values compiled from several literature sources that are listed in Table 2.

Table 2. Position of Stretching Mode Absorption Bands in Mid-Infrared Absorption Spectra of a-SiO_x:H, a-SiO_xN_y:H, and a-SiN_x:H Films on Silicon Wafers, Their Assigned Vibration Modes, and the Respective Proportionality Constant[a]

vibration mode	peak center (cm^{-1})
Si−N, symmetric stretch	470
Si−O, rocking	514
Si−Si, breathing	617
Si−O, bending	811
Si−N, asymmetric stretch	845−870
Si−O, symmetric stretch	980−1080
N−H, rocking	1175
Si−O, asymmetric stretch	1165−1180
$N-H_2$, bending	1540
Si−H, stretch	2000−2220
N−H, stretch	3300−3335

[a]The vibrational mode peak wavenumbers have been compiled from several sources for Si−O[36,37] and S−N, Si−H, and N−H.[38−42]

The absorption intensity (I_N) of the respective stretching modes is proportional to the amount of oxygen, nitrogen, and hydrogen bonded to silicon[42] and was calculated using the following relationship

$$I_N = \int \frac{\alpha(\omega)}{\omega}\, d\omega \quad (1,)$$

where α is the absorption coefficient and ω the wavenumber of the probing energy. The bond densities of the various stretching modes were then calculated as the product of the relevant proportionality constant A (as listed in Table 3) and I_N at the respective vibrational mode frequency.[42]

Table 3. Proportionality Constants and Associated Molecular Groups of Stretching Mode Absorption Bands in Mid-infrared Absorption Spectra of a-SiO_x:H, a-SiO_xN_y:H, and a-SiN_x:H Films on Silicon Wafers

molecular bond associated with stretching mode	proportionality constant, A ($\times 10^{19}$ cm^{-2})
Si−N	2.07[41]
Si−O	1.48[37]
Si−H	22.0[41]
N−H	12.0[41]

2.3. Preparation and Characterization of pn Test Solar Cells.

Test solar cells consisting of a pn heterojunction with both the emitter and absorber contacts on the rear side were used to assess the influence of the interlayers on the solar cell V_{oc} and J_{sc}. Such test solar cells have been successfully used to screen the appropriate doping level of the absorber for use in actual LPC-Si solar cells with a lower resistive but elaborate contacting scheme.[7] Moreover, when illuminated through the glass side, the collection of carriers, generated at the front side is particularly sensitive to the passivation of the buried IL/c-Si interface.

Various interlayer stacks were grown on precleaned 300 × 300 × 3.3 mm^3 borosilicate glass substrates using a PECVD system followed by either a 5 or 10 μm thick intrinsic a-Si:H layer to form the precursor for the absorber as described in detail elsewhere.[4] Absorber p-type doping was achieved by depositing a thin boron doped a-Si:H layer on top of the precursor. The boron from this layer was homogeneously distributed throughout the absorber during liquid-phase crystallization resulting in an acceptor concentration of about 10^{16} cm^{-3}.[4] Prior to LPC, hydrogen effusion is mandatory to prevent blistering of the silicon caused by explosive expulsion of hydrogen by the rapid rate of heating involved. Therefore, after deposition, the glass substrates with the IL/precursor layers were cut into 100 × 100 mm^2 pieces and annealed in three 8 h long stages, each at 450, 550, and then 650 °C under flowing nitrogen to effuse the hydrogen from the a-Si:H. Liquid-phase crystallization of the a-Si:H to polycrystalline silicon c-Si was achieved by sweeping a 30 mm wide continuous wave 808 nm laser beam (LIMO laser) over the silicon in air. Afterward, the LPC-Si was passivated using an active hydrogen plasma in a parallel plate reactor excited at 13.56 MHz with the substrate held at 600 °C. Different parameter sets were used to optimize the hydrogen plasma passivation process as listed in Table 4.

Table 4. Process Parameters for Active Hydrogen Plasma Passivation

parameter	value
temperature (°C)	600
power (W)	50/100
pressure (Pa)	50/250
treatment time (min)	10/30

The treatment time was determined by the duration of the HPP process at 600 °C. After this, the heaters were switched off and the substrates cooled to 300 °C while the hydrogen plasma was still active, avoiding hydrogen effusion, which occurs at temperatures above 400 °C. The chronological temperature profile used during the HPP is shown in Supporting Information (SI) Figure S1.

Optical emission spectroscopy (OES) was used to study the hydrogen plasma, during the passivation process. An optical fiber-based Avantes AvaSpec 2048-2 spectrometer was used to measure the intensities of emission lines from electronically excited hydrogen atoms and molecules in the plasma bulk: the H_α and H_β Balmer lines emitted by H atoms at 656 and 486 nm, respectively, and the $Q_1(2-2)$ line at 622.48 nm by H_2 molecules.[30] The peaks were fitted with Gaussian profiles after subtracting the continuous background originating from the heating lamps.

DOI: 10.1021/acsami.5b05318
ACS Appl. Mater. Interfaces 2015, 7, 19282−19294

After hydrogen passivation, the surface material damaged by ion bombardment was removed by wet chemical etching leaving absorbers with a final thickness of 4.3 and 8.5 μm. Test solar cells without hydrogen passivation were processed in parallel for reference purposes. Next, an intrinsic a-Si:H layer followed by a phosphorus doped n-type a-Si:H layer was deposited on top of the p-type LPC-Si using PECVD. An emitter area of 8 × 2 mm^2 was determined for one set of test solar cells using a ZnO:Al/Ag stack and for the second set, using a sputtered In_2O_3:Sn film. In both cases, the absorber was contacted using evaporated aluminum. A sketch of a test solar cell using ZnO:Al/Ag to contact the emitter is shown in Figure 1.

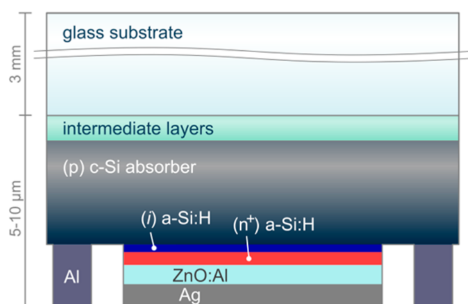

Figure 1. Sketch of a test solar cell with a p-type LPC-Si absorber on glass. The heterojunction i/n emitter was contacted using a ZnO:Al/Ag stack, which also functions as a back-reflector, while the absorber was contacted by an Al layer.

The current−voltage characteristics of the test solar cells were acquired using a class AAA sun simulator (WXS-150-S from Wacom Electric Co, Saitama, Japan) under standard test conditions. Spectral response spectra were acquired on a homemade system equipped with a monochromator from LOT Oriel and used to calculate the external quantum efficiency (EQE) and thus the short circuit current of the structures. Optical losses were determined by measuring the wavelength dependent total test cell reflection (R) using a spectrophotometer (Lambda 1040 by PerkinElmer) equipped with a 150 mm integrating sphere. The R and EQE spectra were used to determine the internal quantum efficiency IQE as IQE = EQE/(1 − R). IQE spectra then gave a qualitative indication of the passivation quality in the test solar cell.

The interface of a glass/IL/Si stack, before and after LPC, was studied using transmission electron microscopy (TEM) on lamella prepared by focused ion beam milling. Selected area electron diffraction patterns of different regions of relatively thick lamella were acquired using a TECNAI G^2 TEM instrument (FEI, Hillsboro, OR, USA). High resolution transmission electron microscopy HRTEM images were acquired on a TITAN instrument on thinner lamella.

3. RESULTS

3.1. PECVD of a-SiO_x:H, a-SiN_x:H, and a-SiO_xN_y:H Interlayers.

The CO_2 and O_2 densities as measured by mass spectrometry of the PECVD exhaust gases are shown in Figure 2 as a function of the plasma RF power. Three different process gas mixtures were used: pure CO_2, an admixture with SiH_4, and an admixture with SiH_4 and N_2. The CO_2 density was derived from the mass spectrum at mass (m) = 44, while the O_2 density is measured at m = 32. A higher CO_2 process gas dissociation was achieved with higher RF powers, resulting in lower measured CO_2 densities (Figure 3). In the case of the pure CO_2 process gas, the only stable molecules in the plasma are CO_2, CO, and O_2. For each dissociated CO_2 molecule, one CO molecule and half of an O_2 molecule are produced. As expected and shown in Figure 2, for a pure CO_2 plasma, the measured molecular oxygen increased by half as the CO_2 density was

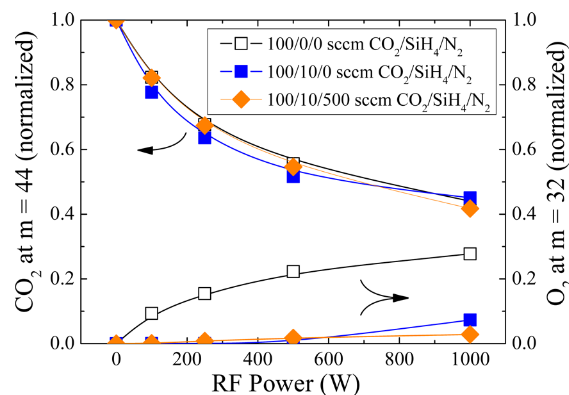

Figure 2. Relative densities of CO_2 and O_2 in dependence of the RF power measured during PECVD by mass spectrometry in the exhaust line for three different gas mixtures (pure CO_2, CO_2/SiH_4, and $CO_2/SiH_4/N_2$). The data are normalized to the pure CO_2 conditions.

decreased by dissociation. The situation changed, when SiH_4 was added to the process gas. The O_2 density decreased to almost zero, indicating a full incorporation of oxygen into the deposited a-SiO_x:H layers for all levels of RF power in this series. Interestingly, the dissociation of CO_2 depended only on the RF power and not on the process gas composition; it only slightly changed when either SiH_4 or N_2 was added to the CO_2 gas flow. This can be explained by the very efficient SiH_4 process gas utilization in the process window considered. For all RF power levels between 100 and 1000 W, the SiH_4 process gas (measured at m = 30 in the mass spectrum) was fully consumed. Therefore, the film growth was limited by the SiH_4 gas flow and neither by the RF power nor by the admixture of CO_2 or N_2.

SiH_4 was also fully consumed in the case of a-SiN_x:H deposition using a mixture of of N_2 and SiH_4 as the process gas. Since the SiH_4 dilution in N_2 was very high (factor of 100−200) compared to that in CO_2, a degree of depletion similar to the one observed for CO_2 could not be detected. Therefore, the N_2 consumption was very low and could not be detected in the large N_2 signal.

3.2. Influence of N_2 and CO_2 Admixture on Deposited Interlayer Material Properties.

The absorption coefficient spectra of various a-SiO_x:H, a-SiN_x:H, and a-SiO_xN_y:H films are presented in SI Figures S2, S3, and S4, respectively. An example of the deconvolved components of an a-SiO_xN_y:H film, used to calculate various bond densities, is shown in SI Figure S5. The bond densities of the Si−N, Si−O, Si−H, and N−H bonds hereafter represented by [Si−N], [Si−O], [Si−H], and [N−H], respectively, of the various a-SiO_x:H, a-SiN_x:H, and a-SiO_xN_y:H films, together with the resultant refractive index at 633 nm (n_{633}) are presented in Table 5.

First, the Si−O stretching bond density of the a-SiO_x:H films only slightly decreased even though [CO_2/SiH_4] was reduced by a factor of 5, indicating that the SiH_4 gas flow rate was the limiting element. Since no Si−H bonds were detected in the a-SiO_x:H films, all of the silicon atoms supplied by SiH_4 combined with oxygen[24,43] leading to an O/Si content close to 2.[37] The refractive index reduced from 1.5 to 1.44 as the CO_2/SiH_4 ratio increased from 5 to 25, thus increasing the O/Si ratio in the films similar to trends observed elsewhere.[27]

All a-SiO_xN_y:H films, grown using a $N_2/CO_2/SiH_4/H_2$ gas mixture, contained hydrogen that was incorporated as Si−H and N−H bonds. The coincidence of Si−H and N−H bonds in

DOI: 10.1021/acsami.5b05318
ACS Appl. Mater. Interfaces 2015, 7, 19282−19294

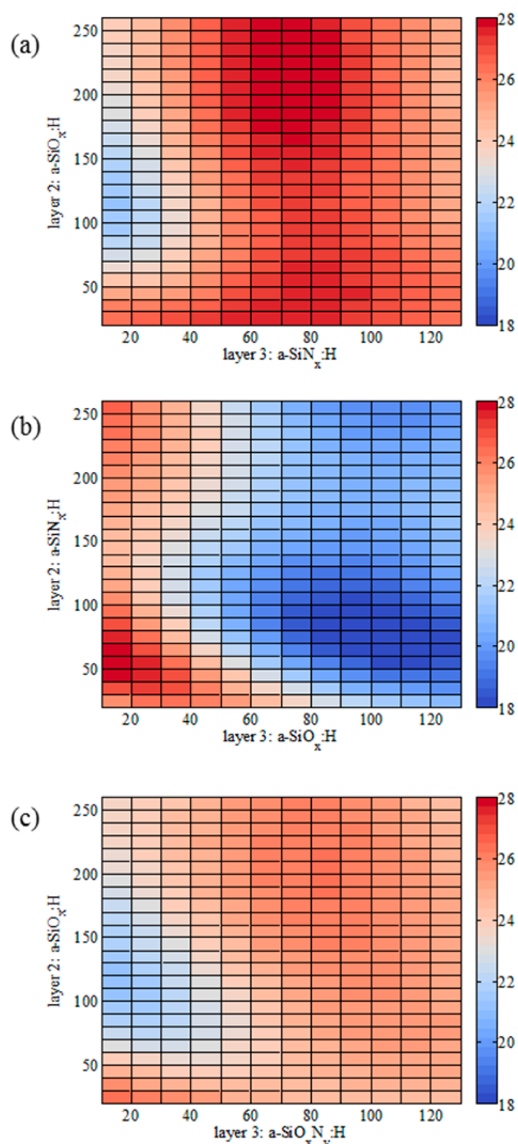

Figure 3. Calculated photocurrent maps as a function of thicknesses, in nanometers, of the second and third layers in various silicon dielectric stacks for (a) NON with layer 1 (a-SiN$_x$:H) thickness fixed at 20 nm, (b) ONO with layer 1 (a-SiO$_x$:H) thickness fixed at 150 nm, and (c) NO(ON) layer 1 (a-SiN$_x$:H) thickness fixed at 20 nm. The photocurrent density in mA/cm^2 is indicated by the vertical scale.

the a-SiO$_x$N$_y$:H films indicates a nitrogen excess in the films.[44] It is notable that for the same $CO_2/SiH_4/H_2$ gas ratio, Si−H bonds were present in the a-SiO$_x$N$_y$:H films but absent in the a-SiO$_x$:H films. n_{633} reduced toward 1.55 with increasing CO_2/SiH_4 ratio, as observed elsewhere[27,45] for the lower N_2 flow of 500 cm^3(STP) min^{-1}. A similar trend was not obvious for the higher N_2 flow of 1000 cm^3(STP) min^{-1} possibly due to complexity of bonding configurations caused by competitive oxidation of silicon caused by a high supply of both nitrogen and oxygen to the deposition process. However, generally for the same CO_2/SiH_4 ratio, the refractive index reduced with N_2 flow.

The a-SiN$_x$:H film grown without H_2 addition to the deposition gas mixture had zero [N−H] indicating a relatively low H content.[40,46] In the absence of H_2, the observed Si−H bonds arose from the silane.[26,46] For a-SiN$_x$:H films grown in the presence of hydrogen, a high N_2/SiH_4 gas flow ratio of 100 resulted in high values of [Si−N] and [N−H], each exceeding 10^{23} cm^{-3}. Since [N−H] exceeded [Si−H], the films were nitrogen rich.[23,26,47,48] Halving the N_2/SiH_4 down to 50 reduced [N−H] by a factor of about four, but [Si−N] remained unchanged. A high value of [N−H] in the order of 10 ^{22} cm^{-3} and above is undesirable because it reduces the a-SiN$_x$:H film density[23] and thus the effectiveness as a diffusion barrier. Also, the refractive index of the a-SiN$_x$:H films reduced from 3.2 to 1.57 when N_2/SiH_4 increased from 50 to 100 indicating an increased nitrogen incorporation in the films.[38,40,46] The a-SiN$_x$:H films made with N_2/SiH_4 = 50 and 60 exhibit n_{633} above 2.0, which corresponds to an N/Si content of the films below 1.3 indicating a nitrogen deficiency.[23] The low but still detectable Si−O bond density in the a-SiN$_x$:H films (grown without intentional addition of CO_2) most probably originates from an oxidized surface.[38,45,49,50] We also observed that if the vacuum was broken after the a-SiN$_x$:H growth, the subsequently grown precursor layer would delaminate.

3.3. Design of Stacked Silicon Dielectric Film Interlayers for LPC-Si Absorbers on Glass. The a-SiO$_x$:H, a-SiO$_x$N$_y$:H, and a-SiN$_x$:H films for application in IL stacks were selected based on a compromise of their properties. Only those films that supported adhesion of the silicon to the glass both before and after laser crystallization were selected for designing the stacked interlayers, and their deposition conditions are summarized in Table 6 for reference purposes.

The absorption coefficient spectra of the optimized a-SiO$_x$:H, a-SiO$_x$N$_y$:H, and a-SiN$_x$:H films used for further investigation of the test solar cells are presented in SI Figure S6. The spectra are split to show the (a) Si−O and Si−N bending and stretching regimes, (b) the Si−H stretching regime, and (c) the N−H stretching regime. The peak absorption coefficient shifted to higher frequencies in moving from a-SiN$_x$:H to a-SiO$_x$N$_y$:H to a-SiO$_x$:H. The Si−H bending modes around 875−945 cm^{-1}[51] were clearly visible for the a-SiO$_x$:H film but partially and completely obscured by the Si−N stretching mode[41,42] for the a-SiO$_x$N$_y$:H and a-SiN$_x$:H films, respectively. Each of the single layers on silicon was further annealed under the same conditions for hydrogen effusion out of the silicon absorber, i.e., up to 650 °C in nitrogen ambient conditions, but the absorption coefficient spectra remained unchanged.

Although the refractive index of the chosen a-SiN$_x$:H layer was too low for perfect antireflection, it provided the best wetting and adhesion of the stack to the glass. Also the values for [N−H], [Si−O], and [Si−H] of the selected a-SiN$_x$:H film (see Table 6) were in the range of values for which a minimal defect density at the a-SiN$_x$:H/Si interface is expected.[26] For the selected a-SiO$_x$:H film, [Si−H] was below the detection level and n_{633} was quite low at 1.44. The shoulder on the higher frequency side of the Si−O stretching mode around 1200 cm^{-1} has been attributed to longitudinal optical modes[52] caused by O atoms vibrating out of phase.[36] The presence of this high shoulder is often an indicator of the oxygen concentration approaching that of the stoichiometric value for SiO_2[36,53] and increased film density.[52] Such a film is a potentially suitable for field effect passivation of both n-type and lightly doped p-type silicon since oxygen incorporation reduces the density of traps at the interface with silicon.[54] Lastly, for the a-SiO$_x$N$_y$:H film, values of both [Si−O] and [Si−N] were below those of the a-SiO$_x$:H and a-SiN$_x$:H films, respectively, with [Si−H] being similar to the a-SiN$_x$:H film and uniquely a rather high value of [N−H] which was not detected in the other two films.

DOI: 10.1021/acsami.5b05318
ACS Appl. Mater. Interfaces 2015, 7, 19282−19294

Table 5. Breakdown of the Refractive Index, the Si–N, Si–O, Si–H, and N–H Bond Densities of a-SiO_x:H, a-SiN_x:H, and a-SiO_xN_y:H Films Grown Using Different [N_2/SiH_4] and/or [CO_2/SiH_4] Ratios during PECVD Deposition[a]

						bond density ($\times10^{22}$ cm^{-3})			
N_2 (cm^3(STP) min^{-1})	CO_2 (cm^3(STP) min^{-1})	[N_2]/[SiH_4]	[CO_2]/[SiH_4]	deposition rate (nm/s)	n_{633}	[Si–N]	[Si–O]	[Si–H]	[N–H]
0	100	0	25	0.27	1.44	0	6.8	0	0
	100	0	10	0.54	1.49	0	6.5	0	0
	50	0	5	0.53	1.55	0	6.2	0	0
500	0	50	0	0.31	3.2	15.0	0.7	0	0.4
	20	50	2	0.44	1.73	2.4	4.8	0.8	0.7
	50	50	5	0.56	1.59	0	7.2	1.4	0.6
	100	50	10	0.54	1.55	0	8.5	1.6	0.6
1000	0	100	0	0.54	1.57	15.6	0.3	1.0	1.6
	50	100	5	0.48	1.65	7.9	5.4	1.6	0.6
	100	100	10	0.49	1.56	7.4	3.8	2.2	0.9
1200	0	60*	0	0.33	2.03	7.9	1.4	0.9	0

[a]Film thickness was roughly 200 nm. All the samples were grown using a hydrogen flow rate of 200 cm^3(STP) min^{-1}, RF power of 600 W, and pressure of 133 Pa with the exception of the one marked with an asterisk (*) which was grown without hydrogen addition and at 250 W and 200 Pa.

Table 6. Process Gas Mixtures, [Si–H], Si–O], [Si–N], and [N–H] for a-SiO_x:H, a-SiO_xN_y:H, and a-SiN_x:H Films with Sufficient Adhesion between Glass and Silicon

				bond density ($\times10^{22}$ cm^{-3})			
dielectric layer	N_2/SiH_4	CO_2/SiH_4	n_{633}	[Si–N]	[Si–O]	[Si–H]	[N–H]
a-SiO_x:H	0	25	1.44	0	6.8	0	0
a-SiN_x:H	60	0	2.03	7.9	1.4	0.9	0
a-SiO_xN_y:H	50	2	1.74	2.4	4.8	0.8	0.7

Three configurations of silicon triple dielectric stacks containing a-SiO_x:H ("O"), a-SiN_x:H ("N"), and a-SiO_xN_y:H ("(ON)") were investigated, namely, the ONO,[5,8,47,55] NON,[56] and an NO(ON) interlayer. An optical simulation routine based on Matlab was used to determine the thickness of each film in the respective triple stack that led to a maximum photocurrent in a glass/IL/9 μm LPC-Si/ZnO:Al/Ag test solar cell. The absorption coefficient and refractive index spectra (see SI Figures S7 and S8, respectively) corresponding to the chosen a-SiO_x:H, a-SiN_x:H, and a-SiO_xN_y:H films were used to calculate the photocurrent under the assumption of negligible recombination losses. The three-dimensional current maps as a function of the thickness of two of the films in the interlayer stack with the thickness of a less critical layer fixed are displayed in Figure 3. The thickness of the first a-SiN_x:H layer in the NON stack was fixed at 20 nm, whereas the thicknesses of the second a-SiO_x:H and the third (a-SiN_x:H) layers were varied. As seen from Figure 3a, the photocurrent of the NON stack was mainly determined by the thickness of the third (a-SiN_y:H) layer. The highest current density of 25 mA/cm^2 was calculated for a third a-SiN_x:H layer thickness range of 60–80 nm.

Since the refractive index of the first a-SiO_x:H layer in the ONO stack was close to that of glass, its thickness had no significant effect on the photocurrent. The thickness of the first a-SiO_x:H layer was chosen to be 150 nm so as to block mobile impurities from the glass. The highest photocurrent of 25 mA/cm^2 was calculated for a second layer (a-SiN_x:H) thickness ranging from 50 to 70 nm and a third layer (a-SiO_x:H) thickness of 10–20 nm. Finally, for the NO(ON) stack, the highest photocurrent of 23 mA/cm^2 was calculated for two different thickness ranges for the second (a-SiO_x:H) layer, namely, 20–30 and 150–250 nm, corresponding to thickness ranges of the third (a-SiO_xN_y:H) layer of 20–30 and 70–100 nm, respectively.

The final thickness of the individual silicon dielectric layers in the NON- and ONO-interlayer triple stacks was easily arrived at as 20/100/80 and 150/60/10 nm, respectively. However, determining the optimal thickness of the individual layers in the NO(ON) stack was more complicated since other factors such as effectiveness of the diffusion barrier and deposition rate had to be considered. For instance, the first thickness set with high calculated photocurrent; i.e., 20/20–30/20–30 nm was disregarded, since it would be insufficient for effective blocking of impurities from the glass. The second optimum of 20/150–250/70–100 nm for the NO(ON) stack would have resulted in a minimum total thickness of 240 nm. Therefore, in order to save deposition time, a total thickness of 200 nm was arrived at by choosing a stack of 20/100/80 nm (a-SiN_x:H/a-SiO_x:H/a-SiO_xN_y:H) giving a slightly lower calculated current density of 22.3 mA/cm^2.

3.4. Effect of Hydrogen Plasma Passivation and Correlation to Passivation Layer Properties. Having chosen three optically acceptable interlayer stacks, we proceeded to test their suitability for passivation of the p-type LPC-Si absorbers using test solar cells. We investigated the influence of HPP for test solar cells with three different types of IL layer stacks by varying RF power (P) and gas pressure (p) of the hydrogen plasma for short (10 min) and long (30 min) HPP as described in section 2.2. The values of V_{oc} measured under AM1.5 global illumination of the test solar cells via the glass side, without HPP and after four different HPP treatments of the LPC-Si absorber, are presented in Figure 4a). In general, RF power and gas pressure had a strong influence on the HPP process. The ratio P/p is a measure of the available energy per H_2 molecule in the plasma and, therefore, also a measure of the ionization and dissociation degree of the process gas H_2. As shown in Figure 4a), the resulting V_{oc} was generally higher for cells with absorbers treated using low P/p conditions. We also investigated the influence of the hydrogen plasma conditions

DOI: 10.1021/acsami.5b05318
ACS Appl. Mater. Interfaces 2015, 7, 19282–19294

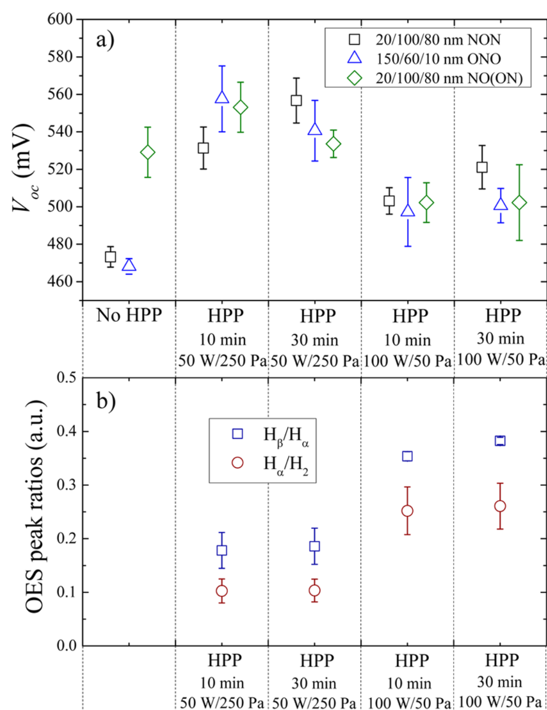

Figure 4. (a) Influence of the HPP conditions on the open circuit voltages of LPC-Si-based solar cells with three different IL stacks; (b) OES peak ratios H_β/H_α and H_α/H_2 measured during the HPP processes. The abbreviations "O", "N", and "(ON)" represent a-SiO_x:H, a-SiN_x:H, and a-SiO_xN_y:H, respectively. Eight test solar cells were considered for each category.

used in this series by means of OES. The resulting emission peak intensity ratios H_β/H_α and the H_α/H_2 are presented in Figure 4b). H_α/H_2 is a measure of the dissociation degree[57] and H_β/H_α a measure of the electron energy.[58] Both ratios increased with P/p and were obviously independent of the treatment time. Since the V_{oc} reduced even when the H atom density increased with P/p, either an additional degradation of the LPC-Si absorber by energetic ions[59] or incorporation of more hydrogen than was necessary to saturate the existing silicon dangling bonds, or both, may have occurred. Although 100−200 nm of the surface region of the LPC-Si absorber were removed by chemical etching after HPP, this degradation may have reached deeper regions of the absorber. Such an observation has been reported previously, whereby a remote hydrogen plasma, i.e., a treatment without direct ion bombardment of the silicon, resulted in higher values of V_{oc} than a direct plasma.[59] The additional damage increased with RF power and pressure and was independent of the treatment time. Another possible reason for reduced passivation at higher H_β/H_α ratio could have been the partial neutralization of the boron dopant in the absorber by hydrogen atoms.[60]

The last layer within the IL stack, being in direct contact with the c-Si absorber, was thus responsible for its surface passivation. We observed that the increase of V_{oc} by the HPP treatment strongly depended on the material properties of this last layer. While the V_{oc} of test solar cells with a-SiO_x:H and a-SiN_x:H passivation layers strongly increased (i.e., about +80 mV) after the HPP treatment, the increase was smaller (about 20 mV) with the a-SiO_xN_y:H passivation layer (Figure 4 a). These test solar cells with the a-SiO_xN_y:H passivation layer had a high V_{oc} exceeding 500 mV even without HPP treatment ,and the final V_{oc} was comparable to the cases with a-SiO_x:H and a-SiN_x:H passivation layers after HPP exposure.

HPP conditions of 50 W and 250 Pa for 10 min reduced the recombination losses within the absorber and its interface and thus increased J_{sc} in the test solar cells. The measured EQE spectra for test solar cells, with and without hydrogen plasma treated c-Si absorbers, are shown in Figure 5.

The test cells were made on two different IL stacks, (a and b) an IL sequence with an a-SiO_x:H passivation layer and (c and d) an IL sequence with an a-SiO_xN_y:H passivation layer, and were provided with a ZnO:Al/Ag back-reflector. The EQE spectra correspond to test cells with two different LPC-Si absorber thicknesses of 4.3 μm in Figure 5a,c and of 8.5 μm in Figure 5b,d. The HPP treatment strongly increased the values of J_{sc} which are indicated next to the respective EQE curves in Figure 5. Similar to V_{oc}, the increase in J_{sc} was strongest for test solar cells with a-SiO_x:H passivation layers, while the recombination losses were already on a low level for test solar cells with a-SiO_xN_y:H passivation layers and no HPP treatment (see also Table 7). The $(1 - R)$ spectra (see Figure 5a−d set the theoretical upper limit for J_{sc} in these test solar cells (see values next to the curves). The area between the $1 - R$ and the EQE spectra corresponds to losses caused by recombination and parasitic optical absorption in the glass, the IL stack, the amorphous i/n emitters, and ZnO:Al/Ag back-reflector. This loss area was smallest for cells with the a-SiO_xN_y:H passivation layer.

The internal quantum efficiency IQE spectra of a 4.3 μm and an 8.5 μm thick c-Si absorber, determined from EQE and $1 - R$, are also shown in Figure 5e,f, respectively. With the a-SiO_xN_y:H passivation layer, the IQE values from 450 to 850 nm exceeded 80% and reduced at longer wavelengths because the indirect band gap of c-Si lies around 1100 nm. Conversely, the IQE values were generally lower with a-SiO_x:H passivation layers causing a J_{sc} loss of 2.4 mA/cm^2 on the 8.5 μm absorbers and even more at 13 mA/cm^2 on the thinner absorber. Since the absorption coefficient of visible light by silicon is very high, the correspondingly low IQE can only be explained by a high surface recombination velocity of photogenerated carriers close to the glass side. Since the surface to volume ratio is reduced in the thicker LPC-Si absorber, the influence of surface recombination losses with respect to bulk recombination reduced and thus carriers generated from longer wavelength photons could be more efficiently collected than in the thinner absorber. The IQE data are therefore proof of the superior surface passivation of the a-SiO_xN_y:H compared to a-SiO_x:H.

3.5. TEM Study of the a-SiO_xN_y:H/c-Si Interface Region.

The preceding NO(ON)-interlayer stack provided an adequate barrier for boron from glass and was successfully implemented in solar cells leading to a photoconversion efficiency of 10.8% using a 4.3 μm thick p-type absorber as reported elsewhere.[4] Additionally, since the wettability of silicon on an a-SiO_xN_y:H surface is below that of a-SiN_x:H but higher than that of a-SiO_x:H,[61] an adequate adhesion of the silicon absorber on the glass after crystallization was guaranteed. In order to investigate how to further improve the NO(ON) IL, we studied the LPC-Si/a-SiO_xN_y:H interface using cross-section TEM.

A comparison of TEM cross-section images of the a-SiO_xN_y:H/Si interface before and after laser crystallization (SI Figure S9) revealed clusters of brighter material visible close to the LPC-Si/IL interface in both cases, and additionally in the a-SiO_x:H layer after laser crystallization. Also, the a-SiO_xN_y:H/Si

DOI: 10.1021/acsami.5b05318
ACS Appl. Mater. Interfaces 2015, 7, 19282−19294

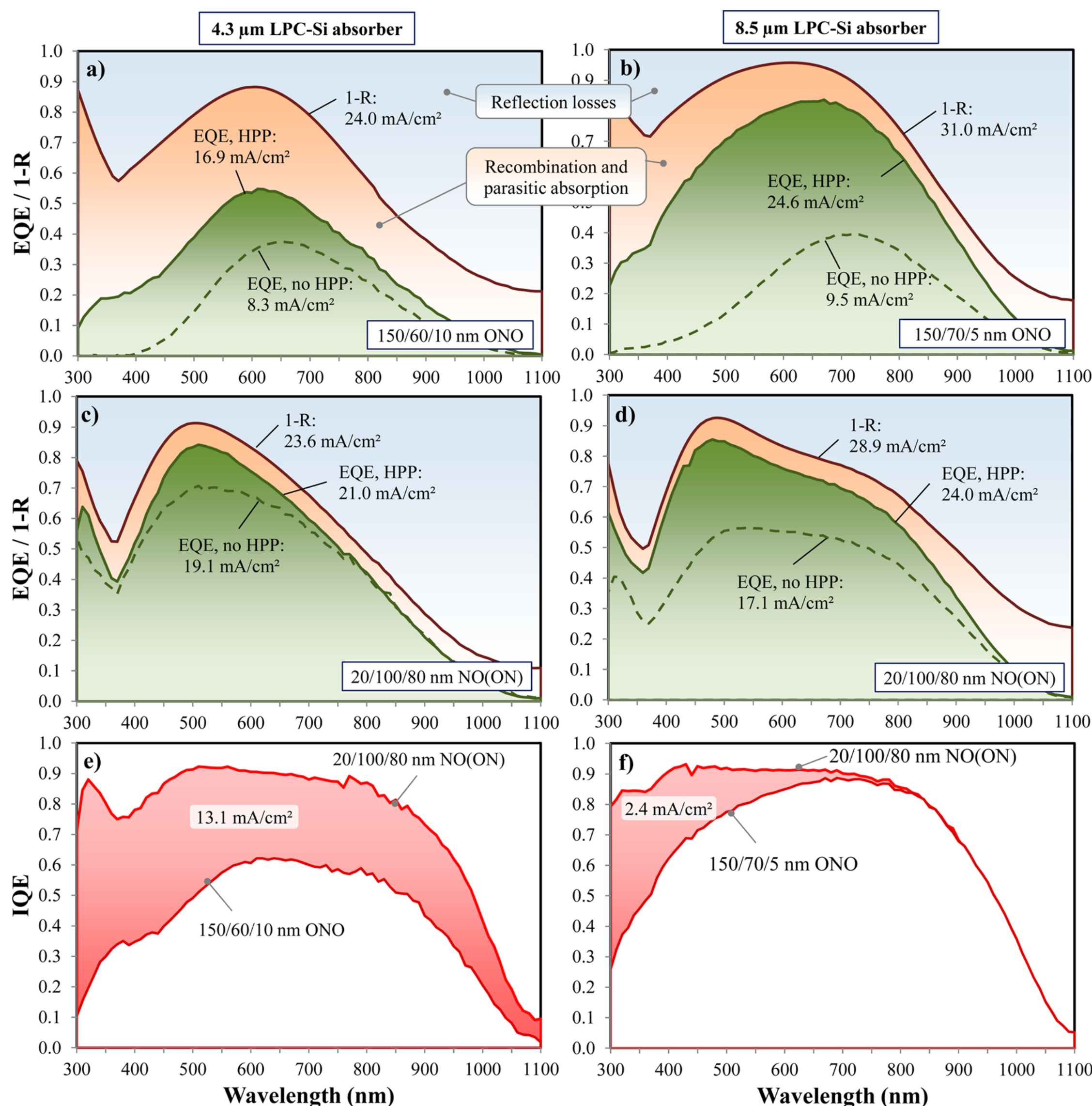

Figure 5. Spectra of measured EQE, without and with hydrogen plasma passivation (HPP) for 30 min at 600 °C, 50 W, and 250 Pa and total reflection (1-R) measured on test solar cells using a ZnO:Al/back-reflector with (a) an ONO/4.3 μm c-Si stack, (b) an ONO/8.5 μm c-Si stack, (c) an NO(ON)/4.3 μm c-Si stack, and (d) an NO(ON)/8.5 μm c-Si stack. Corresponding IQE spectra after HPP are shown in e and f for the 4.3 and 8.5 μm absorbers, respectively. The abbreviations "O", "N" and "(ON)" represent a-SiO_x:H, a-SiN_x:H, and a-SiO_xN_y:H, respectively.

Table 7. V_{oc} and J_{sc} Measured for Test Solar Cells without and with 30 min HPP Treatment at 600 °C, 50 W, and 250 Pa[a]

absorber thickness (nm)	passivation layer	V_{oc} (mV) no HPP	V_{oc} (mV) with HPP	J_{sc} (mA/cm^2) no HPP	J_{sc} (mA/cm^2) with HPP	increase in $V_{oc}J_{sc}$ (%)
4.3	a-SiN_x:H	473 ± 6	556 ± 12	10.0	15.0	76
	a-SiO_x:H	468 ± 4	541 ± 16	8.3	16.9	135
	a-SiO_xN_y:H	529 ± 13	533 ± 7	19.1	21.0	11
8.5	a-SiO_x:H	463 ± 18	518 ± 8	9.5	24.6	190
	a-SiO_xN_y:H	520 ± 13	545 ± 11	17.1	24.0	47

[a] V_{oc} values are represented by the mean and the standard deviation taken from eight test cells.

interface was quite rough and was bounded by an approximately 10 nm wide interfacial region. The uneven LPC-Si/IL interface stems from the roughness of the first a-SiN_x:H film grown on the glass substrate as is common for CVD.[22,48,55] This is attributed to the high sticking coefficient of the SiH_x radicals and the nitrogen atoms from the feed gas as well as the low surface mobility of the depositing species.[22] A TEM micrograph showing a cross-sectional view of the LPC-Si-interlayer interface after liquid-phase crystallization is presented in Figure 6a.The selected area electron diffraction (SAED) patterns corresponding to the LPC-Si, the region near the LPC-Si/a-SiO_xN_y:H interface, and the a-SiO_x:H layer in the interlayer are presented in Figure 6b–d. The SAED patterns confirm the crystalline nature of the silicon absorber and also

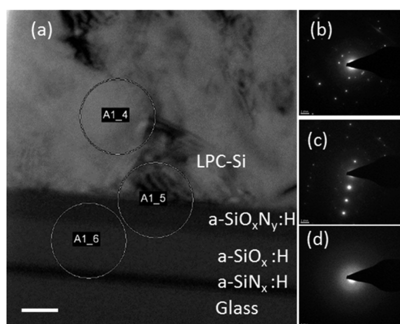

Figure 6. (a) Cross-sectional TEM micrograph of the LPC-Si-interlayer interface after laser crystallization taken on a TECNAI TEM system from a relatively thick lamella. The scale bar is 0.1 μm. (b−d) SAED patterns corresponding to positions A1_4 to A1_6 in panel a.

show that the a-SiO_x:H layer remained purely amorphous after laser crystallization.

Additional cross-section TEM images, taken on a higher resolution instrument and on a thinner lamella of the LPC-Si on the glass stack, after laser crystallization, are presented in Figure 7a−d. The image in Figure 7a is of a similar

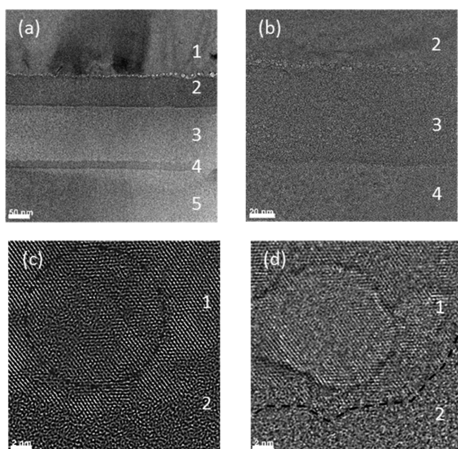

Figure 7. High resolution TEM cross-sectional micrographs of a c-Si-interlayer glass stack, taken on a TITAN instrument from a thinner lamella, showing (a) NO(ON)/c-Si interface after laser crystallization and (b) the a-SiO_x:H/a-SiO_xN_y:H/c-Si region showing clusters close to both interfaces. A detailed view of a cluster containing distorted crystalline lattices in a single-phase matrix, on the silicon side of the interface, is also shown without (c) and with (d) defocusing, respectively. Outlines of a cluster and the interfaces are indicated using dashed lines for clarity. The respective materials are labeled numerically as (1, Si)/(2, a-SiO_xN_y:H)/(3, a-SiO_x:H)/(4, a-SiN_x:H)| (5, glass). The scale bar lengths are 50 nm for a, 20 nm for b, and 2 nm for c and d.

magnification to those of Figure S9a,b, and because of the higher instrument resolution, the clusters at the LPC-Si-interlayer interface are more visible. Moreover under higher magnification (see Figure 7b), other clusters become apparent in the a-SiO_xN_y:H layer close to the a-SiO_x:H interface in the interlayer. The LPC-Si/SiO_xN_y interface which is clearly visible in Figure 7c appears rough but, nevertheless, the LPC-Si grains start growing right from the interface and there is no incubation layer. Additionally Figure 7c shows a nearly circular cluster of mixed-phase LPC-Si (marked out using a dashed line for clarity). With the aid of defocusing, a high contrast image of the spot in Figure 7c could be obtained as shown in Figure 7d. The high contrast HRTEM image, clearly shows the outline of a cluster and a mixture of amorphous and crystalline phases in its interior, while the defocused interface is marked with a dashed line. It also remains to be seen if these clusters introduce electrically active defect sites in the silicon as has been reported elsewhere.[62,63]

The HRTEM images of the LPC-Si-interlayer interface shown in Figure 7c,d confirm that the clusters seen in the lower resolution images (see Figure 7a,c), on the LPC-Si side, are not artifacts. Since the size of the clusters was more pronounced after laser crystallization (compare SI Figure S9c,d), it is plausible that the accompanying hydrogen release may have caused localized amorphization of the silicon.

Although we tested the single barrier layers for hydrogen effusion, this was done at a temperature of 650 °C which is below the temperature during LPC. The LPC process prevailing close to the melting point of silicon may have provided enough thermal energy to break Si−H and N−H bonds in the a-SiO_xN_y:H film. Evidently the single barrier layers need to be tested at 1414 °C to confirm the cause of the clusters observed in TEM. Nevertheless, these results gave us the impetus to reduce the hydrogen (especially N−H bond) content of the a-SiO_xN_y:H layers.

3.6. Optimization of the a-SiO_xN_y:H Passivation Layer.

The mid-IR absorption spectra of the a-SiO_xN_y:H films corresponding to the H_2 flow variation and the RF power variation are shown in SI Figures S10 and S11, respectively. The thickness and refractive index as well as the values of [Si−N], [Si−O], and [Si−H] of various a-SiO_xN_y:H films grown with different plasma power and/or hydrogen flow rate are listed in Table 8. The deposition rate of the a-SiO_xN_y:H film remained almost unchanged when the PECVD hydrogen flow rate was varied from 0 to 200 cm^3(STP) min^{-1}. In this regime, the low SiH_4 flow rate, rather than the etching by hydrogen, appeared to dominate the film growth rate.[58] On the other hand, the refractive index reduced with increasing hydrogen flow rate. Also, although the proportion of hydrogen bonded as N−H increased, the total bonded hydrogen ([N−H] + [Si−H]) *decreased* with increasing hydrogen flow rate. There was, however, no clear trend in [Si−O] and [Si−N] when the hydrogen flow rate was varied.

The deposition rate of the a-SiO_xN_y:H films reduced with increasing plasma power indicating an enhanced plasma etch rate.[58] The value of [Si−O] of the films increased with RF power while [Si−N] decreased at first, and then increased again for the highest power. The dissociation of the CO_2 that increased with RF power has already been shown in Figure1, and since silicon has a higher affinity for oxygen than nitrogen, the Si−O bond density increased. The Si−N bond density only increased for higher power possibly because the O atoms from the CO_2 atoms had been completely consumed by the process allowing the nitrogen to bond with the remaining silicon. This also explains the reduction of the refractive index with increased power as also reported by others.[64] The sum of [N−H] and [Si−H] increased steadily with deposition power mainly as a result of an increase in [Si−H].

The values of J_{sc} and V_{oc}, as well as the product $V_{oc}J_{sc}$, of several test solar cells (glass/NO(ON)/p-type LPC-Si/n-type a-Si emitter with In_2O_3:Sn contacts) for three a-SiO_xN_y:H films, selected from those presented in Table 8, are summarized in Table 9. The V_{oc} did not vary much with or without HPP for all of the test solar cells. Nevertheless, the highest V_{oc} values

DOI: 10.1021/acsami.5b05318
ACS Appl. Mater. Interfaces 2015, 7, 19282−19294

Table 8. Breakdown of the Refractive Index, [Si−N], [Si−O], [Si−H], and [N−H] of a-SiO_xN_y:H Films Deposited with Various H_2 Flow Rates and Excitation Power Levels[a]

power (W)	H_2 (cm^3(STP) min^{-1})	deposition rate (nm/s)	n at 632 nm	bond density (10^{22} cm^{-3}) Si−N	Si−O	Si−H	N−H
600	0	0.56	1.77	8.1	3.8	1.0	0.8
600	50	0.55	1.78	6.0	5.6	0.9	0.8
600	200	0.56	1.79	4.4	6.1	0.4	1.0
600	400	0.52	1.67	7.5	2.0	0.3	1.2
400	200	0.49	1.70	6.4	2.4	0.2	0.7
500	200	0.50	1.77	5.8	4.5	0.3	1.1
600	200	0.56	1.79	4.4	6.1	0.4	1.0
800	200	0.58	1.71	4.1	5.0	1.6	1.0

[a]The SiH_4, CO_2, and N_2 flow rates were fixed at 10, 20, and 500 cm^3(STP) min^{-1}, respectively. The film thickness varied from 230 to 330 nm.

Table 9. Short Circuit Current Density (J_{sc}) and Open Circuit Voltage (V_{oc}) Measured on Test Solar Cells (Glass/NO(ON)/4.3 μm p-Type LPC-Si Absorber/n-a-Si:H Emitter Using In_2O_3:Sn Contacts) for Three Different a-SiO_xN_y:H Passivation Layers with and without Hydrogen Plasma Passivation Conditions of 50 W and 250 Pa at 600 °C for 30 min[a]

PECVD conditions		V_{oc} (mV)		J_{sc} (mA/cm^2)		
power (W)	H_2 (cm^3(STP) min^{-1})	no HPP	with HPP	no HPP	with HPP	improvement in $V_{oc}J_{sc}$ (%)
600	200	510 ± 12	503 ± 16	18.6	18.6	−1
600	50	551 ± 18	564 ± 15	15.2	19.5	31
400	200	500 ± 16	519 ± 36	12.2	17.8	51

[a]V_{oc} values are represented by the mean and the standard deviation taken from six test cells.

around 550−560 mV were attained for the a-SiO_xN_y:H film grown with a low hydrogen flow rate of 50 cm^3(STP) min^{-1} and a power level of 600 W. With the hydrogen flow rate fixed at 200 cm^3(STP) min^{-1}, the V_{oc} with HPP is 520 mV at 400 W and roughly 20 mV higher than that at 600 W but is the same at 500−510 mV, without HPP, for both power levels.

The values of J_{sc} increased for the sample grown with the low H_2 flow of 50 cm^3(STP) min^{-1} and that grown at the low power of 400 W after hydrogen passivation. The highest J_{sc} after passivation was obtained for the film grown at 600 W but with the lowest hydrogen flow rate also leading to the highest $V_{oc}J_{sc}$ product. Although the highest $V_{oc}J_{sc}$ product without HPP was obtained for the a-SiO_xN_y:H grown at 600 W and 200 cm^3(STP) min^{-1} H_2, this value remained unchanged after HPP. The highest increase in the $V_{oc}J_{sc}$ product after HPP was observed for the a-SiO_xN_y:H grown at 600 W and 200 cm^3(STP) min^{-1} H_2, but the absolute $V_{oc}J_{sc}$ product was the lowest of the series.

4. DISCUSSION

Various a-SiO_x:H, a-SiN_x:H and a-SiO_xN_y:H films were grown using PECVD by varying the proportion of CO_2, N_2, and/or H_2 added to the silane deposition gas. Under the high power/low SiH_4 flow conditions used, the [Si−O] in the a-SiO_x:H films reduced only slightly with the CO_2/SiH_4 process gas ratio, and Si−H vibration modes were not detected. The a-SiN_x:H films contained both Si−H and N−H bonds for high N_2/SiH_4 process gas ratios using a RF power of 600 W, while, at 250 W, only Si−H bonds were present. For the a-SiO_xN_y:H films, [Si−O] and [Si−H] increased with the CO_2/SiH_4 ratio regardless of the N_2 flow ratem while, as expected, [Si−N] and [N−H] increased with N_2 flow rate. Also increasing the power with fixed precursor flow rates decreased [Si−N] while [Si−O], [N−H], and [Si−H] increased. With the power kept at 600 W, increasing the H_2 flow rate mainly increased [N−H] while [Si−H] decreased. No clear trend in [Si−O] and [Si−N] was observed under the same conditions.

Three silicon dielectric interlayer stacks were tested in rear side contacted test solar cells, namely, starting from the glass substrate, NON, ONO, and NO(ON), with the last layer in the stack providing the passivation for the p-type LPC-Si absorber. Ideally good passivation should lead to high values of both J_{sc} and V_{oc}. The overall passivation effect using the NON was limited by the low current collection for two reasons. First, the large increase in both J_{sc} and V_{oc}, observed after HPP, proves that the a-SiN_x:H film did not chemically (via H release which reduces defect density) passivate the silicon. This was not surprising considering the absence of N−H bonds and relatively low [Si−H] in the a-Si:N_x:H film as determined from the FTIR analysis. Second, even after hydrogen passivation of the bulk material, the lowest J_{sc} of the films was observed on a-SiN_x:H. Since a-SiN_x:H has a higher dielectric constant than a-SiO_x:H, it develops a higher positive fixed charge.[47] Therefore, field effect passivation via the inversion layer in the p-type silicon with acceptor density of 10^{16} cm^{-3} and higher is limited.[65]

Without HPP, both J_{sc} and V_{oc} with the a-SiO_x:H film at the p-type LPC-Si interface was unexpectedly worse than a-SiN_x:H. Moreover, the drastic increase in both J_{sc} and V_{oc} after hydrogen plasma treatment implies that *both* the a-SiO_x:H films and the bulk c-Si material were chemically passivated via hydrogen diffusion. Thus, the field effect passivation action of the a-SiO_x:H films near the LPC-Si interface was improved by a reduction of the interface traps.

The best silicon interface passivation without hydrogen plasma treatment was observed on a-SiO_xN_y:H compared to a-SiO_x:H and a-SiN_x:H, as verified by the highest J_{sc} and V_{oc} obtained and may be explained by several phenomena. Addition of moderate amounts of nitrogen to a-SiO_x:H reduces the trap density near the interface with silicon by lowering interfacial strain.[66,67] Also, nitrogen addition to a-SiO_x:H to form a-SiO_xN_y:H, reduces the diffusion of boron and other mobile

impurities from other layers into the silicon absorber.[56,67,68] Since there was only a minimal increase in J_{sc} and V_{oc} after HPP, we propose that hydrogen for bulk passivation may have been released from the a-SiO_xN_y:H passivation layer to the silicon during a prior processing step. Since the temperature during laser crystallization was above that of the film deposition, hydrogen was released to the silicon absorber from the a-SiO_xN_y:H layer which contained a higher amount of bonded hydrogen than the a-SiO_x:H and a-SiN_x:H. This suggestion is also supported by the TEM images in which it could be seen that the clusters at the a-SiO_xN_y:H/Si interface enlarged after laser crystallization. Such a scenario is also probable since several studies have demonstrated that, in addition to field effect passivation, silicon dielectric layers with relatively high hydrogen content chemically passivate silicon via hydrogen release during a subsequent heating step.[31,44]

Comparing the chemical bond densities in Tables 6 and 8 with the V_{oc} and J_{sc} values in Tables 7 and 9, respectively, gives a global relationship between the chemical bonding of the passivating layer and the performance of the test cells. Without HPP, increasing [Si−H] in the passivating layer increased both J_{sc} and V_{oc}, in agreement with reports for multicrystalline silicon.[26,69] Spin density measurements have shown that field effect passivation by a-SiO_xN_y:H improves with increasing [Si−H] which reduces interface trap defects in the dielectric film.[21] Additionally values of J_{sc} on both the a-SiN_x:H and the a-SiO_xN_y:H films were higher than that of the a-SiO_x:H film. Moreover, comparing the nitrogen containing films, J_{sc} increased with [N−H] indicating that during LPC-Si, also, the N−H bonds break and contribute hydrogen for passivation of the bulk defects. With additional HPP, J_{sc} and V_{oc} only increased for passivating layers with initially low [Si−H]. Moreover, the degree of increment after HPP was stronger for J_{sc} than for V_{oc}. This together with the enhancement of IQE over a wide spectral range indicates that the HPP mainly increased the diffusion length of the absorber by bulk passivation in agreement with other c-Si solar cells grown on foreign substrates.[59,70] The largest increments in V_{oc} were observed on low hydrogen content passivating layers indicating that a slight reduction in the surface recombination velocity at the interface with silicon may also have reduced the interface trap density. The breaking of N−H bonds is however detrimental to the effectiveness on the field effect passivation since once hydrogen is released, the remaining negatively charged dangling N bonds[25] counteract the positive fixed charge responsible for generating the inversion layer in the p-type LPC-Si.

These results show that for LPC-Si absorbers of up to ~5 μm, a silicon dielectric with the appropriate chemical composition can effectively reduce minority carrier recombination leading to high V_{oc} and J_{sc}. However, for thicker LPC-Si absorbers, additional hydrogen passivation is imperative to reduce recombination in the bulk as also observed for solar cells using multicrystalline wafers.[69]

5. CONCLUSION

We studied the influence of varying the oxidant (CO_2 and N_2) precursor with respect to silane on the properties of a-SiO_x:H, a-SiN_x:H, and a-SiO_xN_y:H films grown by plasma enhanced chemical vapor deposition. Also, the effect of varying the deposition power and hydrogen flow rate during deposition of a-SiO_xN_y:H on Si−H and N−H bond density in the films was investigated. Test heterojunction pn solar cells were used to investigate the influence of the buried interface layer on the passivation of the Si/IL interface and on the hydrogen passivation of the bulk defects. The a-SiO_xN_y:H layer provided a superior field effect passivation at the p-type LPC-Si buried interface (without additional hydrogen plasma passivation) as verified by the higher V_{oc} and J_{sc}, than for the a-SiO_x:H and a-SiN_x:H layers. Reducing the hydrogen flow during the deposition of the a-SiO_xN_y:H films increased [Si−H]/[N−H] and thus both V_{oc} and J_{sc} compared to films grown with higher H_2 flow. Therefore, we demonstrated that the overall reduction in recombination losses by *both* chemical and field effect passivation in solar cells based on thin c-Si on glass depends strongly on the choice of material for buried interface (between the c-Si and glass substrate). Our findings show that a-SiO_xN_y:H film with a high Si−H bond concentration can effectively passivate both the surface and bulk of thin ~4 μm thick c-Si absorbers whereas, for thicker absorbers, additional hydrogen passivation is paramount to achieving high J_{sc}.

■ ASSOCIATED CONTENT

Supporting Information

This material is available free of charge at The Supporting Information is available free of charge on the ACS Publications website at DOI: 10.1021/acsami.5b05318.

Substrate temperature profile during hydrogen plasma passivation, infrared absorption coefficient spectra of all silicon dielectric films discussed in the study, visible wavelength spectra of optical constants for silicon dielectric films used for solar cells, and TEM images comparing buried silicon interface before and after liquid-phase crystallization (PDF)

■ AUTHOR INFORMATION

Corresponding Author

*Phone: +49 30 8062 15675. Fax: +49 30 8062 15677. E-mail: sonya.calnan@helmholtz-berlin.de.

Funding

Financial support was provided by the German Federal Ministry of Education and Research (BMBF) and the state government of Berlin (SENBWF) in the framework of the program "Spitzenforschung und Innovation in den Neuen Ländern" (Grant No. 03IS2151) and by the German Federal Ministry for Economic Affairs and Energy (BMWi) in the "DEMO14" project (Grant No. 0325237).

Notes

The authors declare no competing financial interest.

■ ACKNOWLEDGMENTS

We are grateful to Mr. S. Selve of ZELMI, Technische Universität Berlin for acquiring the TEM data. We thank A. Opitz, H. Rhein, and K. Bhatti for their help with sample preparation. M. Zelt, K. Mack, T. Rückwaldt, and T. Hänel are also thanked for taking various measurements on the samples.

■ REFERENCES

(1) Schmidl, G.; Andrä, G.; Bergmann, J.; Gawlik, A.; Höger, I.; Anders, S.; Schmidl, F.; Tympel, V.; Falk, F. CW-Diode Laser Crystallization of Sputtered Amorphous Silicon on Glass, SiN_x, and SiO_2 Intermediate Layers. *J. Mater. Sci.* **2013**, *48*, 4177−4182.

(2) Green, M.; Basore, P.; Chang, N.; Clugston, D.; Egan, R.; Evans, R.; Hogg, D.; Jarnason, S.; Keevers, M.; Lasswell, P.; O'Sullivan, J.; Schubert, U.; Turner, A.; Wenham, S. R.; Young, T. Crystalline Silicon

on Glass (CSG) Thin-Film Solar Cell Modules. *Sol. Energy* **2004**, *77*, 857–863.

(3) Amkreutz, D.; Müller, J.; Schmidt, M.; Hänel, T.; Schulze, T. Electron-Beam Crystallized Large Grained Silicon Solar Cell on Glass Substrate. *Prog. Photovoltaics* **2011**, *19*, 937–945.

(4) Gabriel, O.; Frijnts, T.; Calnan, S.; Ring, S.; Kirner, S.; Opitz, A.; Rothert, I.; Rhein, H.; Zelt, M.; Bhatti, K.; Zollondz, J. H.; Heidelberg, A.; Haschke, J.; Amkreutz, D.; Gall, S.; Friedrich, F.; Stannowski, B.; Rech, B.; Schlatmann, R. PECVD Intermediate and Absorber Layers Applied in Liquid-Phase Crystallized Silicon Solar Cells on Glass Substrates, IEEE. *J. Photovolt.* **2014**, *4*, 1343–1348.

(5) Dore, J.; Evans, R.; Schubert, U.; Eggleston, B. D.; Ong, D.; Kim, K.; Huang, J.; Kunz, O.; Keevers, M.; Egan, R.; Varlamov, S.; Green, M. A. Thin-Film Polycrystalline Silicon Solar Cells Formed by Diode Laser Crystallization. *Prog. Photovoltaics* **2013**, *21*, 1377–1383.

(6) Dore, J.; Ong, D.; Varlamov, S.; Egan, R.; Green, M. A. Progress in Laser-Crystallised Thin Film Polycrystalline Silicon Solar Cells: Intermediate Layers, Light Trapping and Metallisation. *IEEE J. Photovolt.* **2014**, *4*, 33–39.

(7) Haschke, J.; Amkreutz, D.; Korte, L.; Ruske, F.; Rech, B. Towards Wafer Quality Crystalline Silicon Thin Film Solar Cells on Glass. *Sol. Energy Mater. Sol. Cells* **2014**, *128*, 190–197.

(8) Haschke, J.; Amkreutz, D.; Frijnts, T.; Kuhnapfel, S.; Hanel, T.; Rech, B. Influence of Barrier and Doping Type on the Open-Circuit Voltage of Liquid Phase-Crystallized Silicon Thin-Film Solar Cells on Glass. *IEEE J. Photovoltaics* **2015**, *5*, 1001–1005.

(9) Dore, J.; Varlamov, S.; Green, M. A. Intermediate Layer Development for Laser-Crystallised Thin Film Silicon Solar Cells on Glass. *IEEE J. Photovolt.* **2015**, *5*, 9–16.

(10) Becker, C.; Amkreutz, D.; Sontheimer, T.; Preidel, V.; Lockau, D.; Haschke, J.; Jogschies, L.; Klimm, C.; Merkel, J.; Plocica, P.; Steffens, S.; Rech, B. Polycrystalline Silicon Thin-Film Solar Cells: Status and Perspectives. *Sol. Energy Mater. Sol. Cells* **2013**, *119*, 112–123.

(11) Varlamov, S.; Dore, J.; Evans, R.; Ong, D.; Eggleston, B.; Kunz, O.; Schubert, U.; Young, T.; Huang, J.; Soderstrom, T.; Omaki, K.; Kim, K.; Teal, A.; Jung, M.; Yun, J.; Pakhuruddin, Z.; Egan, R.; Green, M. A. Polycrystalline Silicon on Glass Thin-Film Solar Cells: A Transition from Solid-Phase to Liquid-Phase Crystallised Silicon. *Sol. Energy Mater. Sol. Cells* **2013**, *119*, 246–255.

(12) Kühnapfel, S.; Nickel, N. H.; Gall, S.; Klaus, M.; Genzel, C.; Rech, B.; Amkreutz, D. Preferential {100} Grain Orientation in 10 Micrometer-Thick Laser Crystallized Multicrystalline Silicon on Glass. *Thin Solid Films* **2015**, *576*, 68–74.

(13) Steffens, S.; Becker, C.; Amkreutz, D.; Klossek, A.; Kittler, M.; Chen, Y. Y.; Schnegg, A.; Klingsporn, M.; Abou-Ras, D.; Lips, K.; Rech, B. Impact of Dislocations and Dangling Bond Defects on the Electrical Performance of Crystalline Silicon Thin Films. *Appl. Phys. Lett.* **2014**, *105*, 022108.

(14) Werner, J.; Dassow, R.; Rinke, T.; Köhler, J.; Bergmann, R. From Polycrystalline to Single Crystalline Silicon on Glass. *Thin Solid Films* **2001**, *383*, 95–100.

(15) Wong, J.; Huang, J.; Varlamov, S.; Green, M. A.; Keevers, M. The Roles of Shallow and Deep Levels in the Recombination Behavior of Polycrystalline Silicon on Glass Solar Cells. *Prog. Photovoltaics* **2012**, *20*, 915–922.

(16) Kittler, M.; Seifert, W.; Arguirov, T.; Tarasov, I.; Ostapenko, S. Room-Temperature Luminescence and Electron Beam-Induced Current (EBIC) Recombination Behaviour of Crystal Defects in Multicrystalline Silicon. *Sol. Energy Mater. Sol. Cells* **2002**, *72*, 465–472.

(17) Doshi, P.; Jellison, G. E.; Rohatgi, A. Characterisation and Optimisation of Absorbing Plasma-Enhanced Chemical Vapour Deposited Antireflection Coatings for Silicon Photovoltaics. *Appl. Opt.* **1997**, *36*, 7826–7837.

(18) Stannowski, B.; Gabriel, O.; Calnan, S.; Frijnts, T.; Heidelberg, A.; Neubert, S.; Kirner, S.; Ring, S.; Zelt, M.; Rau, B.; Zollondz, J. H.; Bloess, H.; Schlatmann, R.; Rech, B. Achievements and Challenges in Thin Film Silicon Module Production. *Sol. Energy Mater. Sol. Cells* **2013**, *119*, 196–203.

(19) Amkreutz, D.; Haschke, J.; Kuhnapfel, S.; Sonntag, P.; Rech, B. Silicon Thin-Film Solar Cells on Glass with Open-Circuit Voltages Above 620 mV Formed by Liquid-Phase Crystallisation. *IEEE J. Photovoltaics* **2014**, *4*, 1496–1501.

(20) Kerr, J. A. In *Handbook of Chemistry and Physics*, 77th ed.; Lide, D. R., Ed.; CRC Press: Boca Raton, FL, USA, 1997; Section 9, pp 51–69.

(21) Nguyen, S.; Landford, W.; Rieger, P. Variation of Hydrogen Bonding, Depth Profiles and Spin Density in Plasma Deposited Silicon Nitride and Oxynitride Film with Deposition Mechanism. In *Symposium Proceedings 7th International Symposium on Plasma Chemistry*; Eindhoven, The Netherlands, July 1–5, 1985; Timmermans, C. J., Ed.; Subcommittee of Plasma Chemistry, International Union of Pure and Applied Chemistry: Research Triangle Park, NC, USA, 1985; pp 56–61.

(22) Smith, D. L.; Alimonda, A.; von Preissig, F. J. Mechanism of SiN_xH_y Deposition from N_2-SiH_4 Plasma. *J. Vac. Sci. Technol., B: Microelectron. Process. Phenom.* **1990**, *8*, 551–557.

(23) Parsons, G. N.; Souk, J.; Batey, J. Low Hydrogen Content Stoichiometric Silicon Nitride Films Deposited by Plasma Enhanced Chemical Vapor Deposition. *J. Appl. Phys.* **1991**, *70*, 1553–1560.

(24) Hattangady, S. V.; Alley, R. G.; Fountain, G. G.; Markunas, R. J.; Lucovsky, G.; Temple, D. Effect of RF Power on Remote Plasma Deposited SiO_2 Films. *J. Appl. Phys.* **1993**, *73*, 7635–7642.

(25) Habraken, F. H. P. M.; Kuiper, A. E. T. Silicon Nitride and Oxynitride Films. *Mater. Sci. Eng., R* **1994**, *12*, 123–175.

(26) Mäckel, H.; Lüdemann, R. Detailed Study of the Composition of Hydrogenated SiN_x Layers for High-Quality Silicon Surface Passivation. *J. Appl. Phys.* **2002**, *92*, 2602–2609.

(27) Ay, F.; Aydinli, A. Comparative Investigation of Hydrogen Bonding in Silicon Based PECVD Grown Dielectrics for Optical Waveguides. *Opt. Mater.* **2004**, *26*, 33–46.

(28) Sichanugrist, P.; Sasaki, T.; Asano, A.; Ichikawa, Y.; Sakai, H. Amorphous Silicon Oxide and its Application to Metal/n-i-p/ITO Type a-Si Solar Cells. *Sol. Energy Mater. Sol. Cells* **1994**, *34*, 415–422.

(29) Cuony, P.; Alexander, D.; Perez-Wurfl, I.; Despeisse, M.; Bugnon, G.; Boccard, M.; Söderström, T.; Hessler-Wyser, A.; Hébert, C.; Ballif, C. Silicon Filaments in Silicon Oxide for Next-Generation Photovoltaics. *Adv. Mater.* **2012**, *24*, 1182–1186.

(30) Gabriel, O.; Kirner, S.; Klingsporn, M.; Friedrich, F.; Stannowski, B.; Schlatmann, R. On the Plasma Chemistry during Plasma Enhanced Chemical Vapor Deposition of Microcrystalline Silicon Oxides. *Plasma Processes Polym.* **2015**, *12*, 82–91.

(31) Sritharathikhun, J.; Banerjee, C.; Otsubo, M.; Sugiura, T.; Yamamoto, H.; Sato, T.; Limmanee, A.; Yamada, A.; Konagai, M. Surface Passivation of Crystalline and Polycrystalline Silicon using Hydrogenated Amorphous Silicon Oxide Film. *Jpn. J. Appl. Phys.* **2007**, *46*, 3296–3300.

(32) Theiss, W. *Scout Tutorial 1*, 2012, http://www.wtheiss.com/docs/scout_tutorial1.pdf.

(33) O'Leary, S.; Johnson, S.; Lim, P. The Relationship Between the Distribution of Electronic States and the Optical Absorption Spectrum of an Amorphous Semiconductor: An Empirical Analysis. *J. Appl. Phys.* **1997**, *82*, 3334–3340.

(34) Brendel, R.; Bormann, D. An Infrared Dielectric Function Model for Amorphous Solids. *J. Appl. Phys.* **1992**, *71*, 1–6.

(35) Wojdyr, M. *Fityk*: A General-Purpose Peak Fitting Program. *J. Appl. Crystallogr.* **2010**, *43*, 1126–1128.

(36) Pai, P.; Chao, S.; Takagi, Y.; Lucovsky, G. Infrared Spectroscopic Study of SiO_x Films Produced by Plasma Enhanced Chemical Vapour Deposition. *J. Vac. Sci. Technol., A* **1986**, *4*, 689–694.

(37) He, L.; Inokuma, T.; Kurata, Y.; Hasegawa, S. Vibrational Properties of SiO and SiH in Amorphous SiO_x:H Films ($0 < x < 2.0$) Prepared by Plasma-Enhanced Chemical Vapor Deposition. *J. Non-Cryst. Solids* **1995**, *185*, 249–261.

(38) Taft, E. A. Characterisation of Silicon Nitride Films. *J. Electrochem. Soc.* **1971**, *118*, 1341–1346.

(39) Lanford, W. A.; Rand, M. J. The Hydrogen Content of Plasma Deposited Silicon Nitride. *J. Appl. Phys.* **1978**, *49*, 2473−2477.
(40) Sasaki, G.; Kondo, M.; Fujita, S.; Sasaki, A. Properties of Chemically Vapour Deposited Amorphous SiN_x Alloys. *Jpn. J. Appl. Phys.* **1982**, *21*, 1394−1399.
(41) Bustarret, E.; Bensouda, M.; Habrard, M. C.; Bruyere, J. C.; Poulin, S.; Gujrathi, S. C. Configurational Statistics in a-$Si_xN_yH_z$ Alloys: A Quantitative Bonding Analysis. *Phys. Rev. B: Condens. Matter Mater. Phys.* **1988**, *38*, 8171−8184.
(42) Hasegawa, S.; Anbutsu, H.; Kurata, Y. Connection between Si−N and Si−H Vibrational Properties in Amorphous SiN_x: H Films. *Philos. Mag. B* **1989**, *59*, 365−375.
(43) Smith, D. L. Controlling the Plasma Chemistry of Silicon Nitride and Oxide Deposition from Silane. *J. Vac. Sci. Technol., A* **1993**, *11*, 1843−1850.
(44) Denisse, C. M. M.; Troost, K. Z.; Habraken, F. H. P. M.; van der Weg, W. F.; Hendriks, M. Annealing of Plasma Silicon Oxynitride Films. *J. Appl. Phys.* **1986**, *60*, 2543−2547.
(45) Holloway, P. H.; Stein, H. J. Quantitative Detection of Oxygen in Silicon Nitride on Silicon. *J. Electrochem. Soc.* **1976**, *123*, 723−726 (Solid State Science and Technology—Technical Papers).
(46) Stein, H. J.; Wegener, H. A. R. Chemically Bound Hydrogen in CVD Si_3N_4: Dependence on NH_3/SiH_4 Ratio and on Annealing. *J. Electrochem. Soc.* **1977**, *124*, 908−912 (Solid State Science and Technology—Technical Papers).
(47) Ma, Y.; Yasuda, T.; Lucovsky, G. Fixed and Trapped Charges at Oxide−Nitride−Oxide Heterostructure Interfaces Formed by Remote Plasma Enhanced Chemical Vapor Deposition. *J. Vac. Sci. Technol., B: Microelectron. Process. Phenom.* **1993**, *11*, 1533−1540.
(48) Karabacak, T.; Zhao, Y. P.; Wang, G. C.; Lu, T. M. Growth Front Roughening in Silicon Nitride Films by Plasma Enhanced Chemical Vapour Deposition. *Phys. Rev. B: Condens. Matter Mater. Phys.* **2002**, *66*, 075329-1−075329-10.
(49) Raider, S. I.; Flitsch, R.; Aboaf, J.; Pliskin, W. A. Surface Oxidation of Silicon Nitride Films. *J. Electrochem. Soc.* **1976**, *123*, 560−565.
(50) Blech, M.; Laades, A.; Ronning, C.; Schroeter, B.; Borschel, C.; Rzesanke, D.; Lawerenz, A. *Detailed Study of PECVD Silicon Nitride and Correlation of Various Characterisation Techniques*. In *Proceedings of the 24th European Photovoltaic Solar Energy Conference*, Hamburg, Germany, Sep. 21−25, 2009; WIP: Munich, Germnay, 2009, pp 507−511, DOI: 10.4229/24thEUPVSEC2009-1CV.4.30.
(51) Langford, A. A.; Fleet, M. L.; Nelson, B. P.; Lanford, W. A.; Maley, N. Infrared Absorption Strength and Hydrogen Content of Hydrogenated Amorphous Silicon. *Phys. Rev. B: Condens. Matter Mater. Phys.* **1992**, *45*, 13367−13377.
(52) Diebold, A. C.; Venables, D.; Chabal, Y.; Muller, D.; Weldon, M.; Garfunkel, E. Characterisation and Production Metrology of Thin Transistor Gate Oxide Films. *Mater. Sci. Semicond. Process.* **1999**, *2*, 103−14.
(53) Pliskin, W. A. Comparison of Properties of Dielectric Films Deposited by Various Methods. *J. Vac. Sci. Technol.* **1977**, *14*, 1064−1081.
(54) Moazzami, R.; Hu, C. A High-Quality Stacked Thermal/LPCVD Gate Oxide Technology for ULSI. *IEEE Electron Device Lett.* **1993**, *14*, 72−73.
(55) Hönlein, W.; Reisinger, H. ONO Technology. *Appl. Surf. Sci.* **1989**, *39*, 178−191.
(56) Niimi, H.; Lucovsky, G. Monolayer-Level Controlled Incorporation of Nitrogen in Ultrathin Gate Dielectrics Using Remote Plasma Processing: Formation of stacked ″N-O-N″ gate dielectrics. *J. Vac. Sci. Technol., B: Microelectron. Process. Phenom.* **1999**, *17*, 2610−2621.
(57) Lavrov, B.; Lang, N.; Pipa, A.; Röpcke, J. On Determination of the Degree of Dissociation of Hydrogen in Non-equilibrium Plasmas by Means of Emission Spectroscopy: Experimental Verification. *Plasma Sources Sci. Technol.* **2006**, *15*, 147−155.
(58) Matsuda, A.; Takai, M.; Nishimoto, T.; Kondo, M. Control of Plasma Chemistry for Preparing Highly Stabilized Amorphous Silicon at High Growth Rate. *Sol. Energy Mater. Sol. Cells* **2003**, *78*, 3−26.
(59) Qiu, Y.; Kunz, O.; Fejfar, A.; Ledinsky, M.; Chan, B. T.; Gordon, I.; Van Gestel, D.; Venkatachalm, S.; Egan, R. On the Effects of Hydrogenation of Thin Film Polycrystalline Silicon: A Key Factor To Improve Heterojunction Solar Cells. *Sol. Energy Mater. Sol. Cells* **2014**, *122*, 31−39.
(60) Pankove, J. I.; Wance, R. O.; Berkeyheiser, J. E. Neutralization of Acceptors in Silicon by Atomic Hydrogen. *Appl. Phys. Lett.* **1984**, *45*, 1100−1102.
(61) Li, J.; Hausner, H. H. Influence of Oxygen Partial Pressure on the Wetting Behaviour of Silicon Nitride by Molten Silicon. *J. Eur. Ceram. Soc.* **1992**, *9*, 101−105.
(62) Johnson, N. M. p.; Ponce, F.; Street, R.; Nemanich, R. Defects in Single-Crystal Silicon Induced by Hydrogenation. *Phys. Rev. B: Condens. Matter Mater. Phys.* **1987**, *35*, 4166−4169.
(63) Nickel, N. H.; Anderson, G. B.; Johnson, N. M.; Walker, J. Nucleation of Hydrogen-Induced Platelets in Silicon. *Phys. Rev. B: Condens. Matter Mater. Phys.* **2000**, *62*, 8012−8015.
(64) Hattangady, S. V.; Niimi, H.; Lucovsky, G. Integrated Processing of Silicon Oxynitride Films by Combined Plasma and Rapid Thermal Processing. *J. Vac. Sci. Technol., A* **1996**, *14*, 3017−3023.
(65) Seiffe, J.; Gautero, L.; Hofmann, M.; Rentsch, J.; Preu, R.; Weber, S.; Eichel, R. A. Surface Passivation of Crystalline Silicon by Plasma-Enhanced Chemical Vapor Deposition Double Layers of Silicon-Rich Silicon Oxynitride and Silicon Nitride. *J. Appl. Phys.* **2011**, *109*, 034105-1−034105-12.
(66) Hori, T.; Iwasaki, H.; Tsuji, K. Charge-Trapping Properties of Ultrathin Nitrided Oxides Prepared by Rapid Thermal Annealing. *IEEE Trans. Electron Devices* **1988**, *35*, 904−910.
(67) Green, M. L.; Gusev, E. P.; Degraeve, R.; Garfunkel, E. L. Ultrathin (< 4 nm) SiO_2 and Si-O-N Gate Dielectric Layers for Silicon Microelectronics: Understanding the Processing, Structure, and Physical and Electrical Limits. *J. Appl. Phys.* **2001**, *90*, 2057−2121.
(68) Wu, Y.; Niimi, H.; Yang, H.; Lucovsky, G.; Fair, R. B. Suppression of Boron Transport out of p+ Polycrystalline Silicon at Polycrystalline Silicon Dielectric Interfaces. *J. Vac. Sci. Technol., B: Microelectron. Process. Phenom.* **1999**, *17*, 1813−1822.
(69) Soppe, W.; Hong, J.; Kessels, W.; van de Sanden, M.; Arnoldbik, W.; Schlemm, H.; Devilee, C.; Rieffer, H.; Schiemeier, S.; Bultman, J.; Weeber, A. On Combining Surface and Bulk Passivation of SiN_x:H Layers for mc-Si Solar Cells. *Photovoltaics Specialists Conference, 2002. Conference Record of the Twenty-Ninth IEEE*, New Orleans, LA, USA, May 19−24, 2002; Institute of Electrical and Electronics Engineers: New York, 2002; pp 158−161.
(70) Keevers, M. I.; Turner, A.; Schubert, U.; Basore, P. A.; Green, M. A. Remarkably Effective Hydrogenation of Crystalline Silicon on Glass Modules. In *Proceedings of the 20th European Photovoltaic Solar Energy Conference (PVSEC '05)*, Barcelona, Spain, Jun. 6−10, 2005; WIP: Munich, Germany, 2005; pp 1305−1308.

DOI: 10.1021/acsami.5b05318
ACS Appl. Mater. Interfaces 2015, 7, 19282−19294